Swansea University
Prifysgol Abertawe

Cronfa
Setting Research Free

Cronfa - Swansea University Open Access Repository

_____

This is an author produced version of a paper published in :
Physical Review Letters

_____

Cronfa URL for this paper:
http://cronfa.swan.ac.uk/Record/cronfa28884

_____

Paper:

Dumazer, G., Sandnes, B., Ayaz, M., Maloy, K. & Flekkoy, E. (2016). Frictional fluid dynamics and plug formation in
multiphase millifluidic flow. *Physical Review Letters, 117*(028002)

http://dx.doi.org/10.1103/PhysRevLett.117.028002

_____

Frictional Fluid Dynamics and Plug Formation in Multiphase Millifluidic Flow

Guillaume Dumazer,[1] Bjørnar Sandnes,[2] Monem Ayaz,[1] Knut Jørgen Måløy,[1] and Eirik Grude Flekkøy[1]

[1] *Department of Physics, University of Oslo, P.O. Box 1048 Blindern Oslo, Norway*

[2] *College of Engineering, Swansea University, Bay Campus, Swansea SA1 8EN, United Kingdom**

We study experimentally the flow and patterning of a granular suspension displaced by air inside a narrow tube. The invading air-liquid interface accumulates a plug of granular material that clogs the tube due to friction with the confining walls. The gas percolates through the static plug once the gas pressure exceeds the pore capillary entry pressure of the packed grains, and a moving accumulation front is reestablished at the far side of the plug. The process repeats, such that the advancing interface leaves a trail of plugs in its wake. Further, we show that the system undergoes a fluidization transition — and complete evacuation of the granular suspension — when the liquid withdrawal rate increases beyond a critical value. An analytical model of the stability condition for the granular accumulation predicts the flow regime.

Complex multiphase flows in channels and tubes occur in a range of geophysical, biological, and engineered processes. Examples include transport of blood cells suspended in plasma through the cardiovascular network [1, 2], conveying of powders and granular materials in civil and chemical engineering [3, 4], and transport of oil, gas, and sand through sub-sea pipelines [5]. Even the simple case of two-phase air and water flow through tubes and capillaries displays complex flow behavior, with commonly observed transitions between stratified, bubbly, slug and annular flow depending on the flow rates of the respective phases [6–8]. Hydraulic and pneumatic conveying of particulates and granular materials similarly show a range of flow regimes ranging from bed load, to slug flow, and dilute flow depending on granular loading and fluid flow rate [3, 9–13].

The flow of dense granular suspensions has proved challenging to characterize due in part to the frictional contact interactions between grains, and between grains and the confining boundaries. Examples of complex flow behavior associated with frictional fluid dynamics include shear thinning, shear thickening, shear banding, plug ,growth, and normal stresses [14–18]. Several factors need to be taken into account in order to describe the rheology of dense granular suspensions corresponding to vanishing values for viscous and inertial numbers [16, 19]. The extended contact time between particles introduces Coulomb friction as a dominating dissipation mechanism [15, 17]. Gravity has been shown to play an important part in inducing granular contact dynamics below close packing densities, leading to system spanning contact networks and yield stresses [14].

Discontinuous shear thickening (DST), where increased shear rate causes a sudden jump in the stress producing solidlike behavior, is a striking example of complex frictional fluid dynamics. Recent studies have pointed to both frictional contact dynamics as well as dilation and confinement as the dominating mechanisms for DST [17, 18, 20]. Dilation is the expansion of the granular packing due to shear, which, when confined by system boundaries, causes additional normal stress and friction.

The role of the confining geometry is therefore of fundamental importance in governing the frictional fluid flow behavior at the point where system-spanning contact networks emerge. These grain-grain contact networks mediate imposed stresses through force chains within the packing [20, 21], amplifying the stresses on the boundaries, leading to nonlinear frictional responses [22, 23]. The flow dynamics of granular particles approaching the jamming transition can be described by nonlocal rheological effects in part due to the confinement [24, 25]. In experimental systems, the boundaries are often the confining plates of a rheometer or a flow cell, or the solid walls of a tube. Note, however, that in the case of multiphase flows, the meniscus between immiscible fluids constitutes another type of system boundary. Here the capillary forces acting at the fluid-fluid-grain contact lines impose confining stresses on the granular phase [26].

It is therefore perhaps not surprising to find that multiphase granular or frictional flow in confined geometries are a rich source of spectacular flow instabilities and pattern formation processes. For the case of granular suspension flow in 2D Hele-Shaw geometries these include viscous fingers in granular suspensions [27, 28], labyrinths and frictional fingers [26, 29, 30], stick-slip gas bubbles [30–32], and gas driven fracturing in saturated granular packings [28, 30, 33–38]. The complexity of flow behavior stems from the variety of forces at play (pressure, viscous, capillary, frictional, and gravitational) in addition to effects associated with the confining geometry and inherent system disorder.

Here we focus on a simple model system of confined, multiphase frictional flow: a 1.0 m long glass tube filled with a mixture of glass beads and water, where the tube diameter ($D = 2.0$ mm) is close to the capillary length of the liquid. The granular material settles out of suspension, and the gas invasion dynamic is governed in part by the Coulomb friction associated with granular accumulation fronts ahead of the meniscus [23, 29]. We show that capillary and frictional forces combine to produce a characteristic flow pattern whereby plugs of grains are
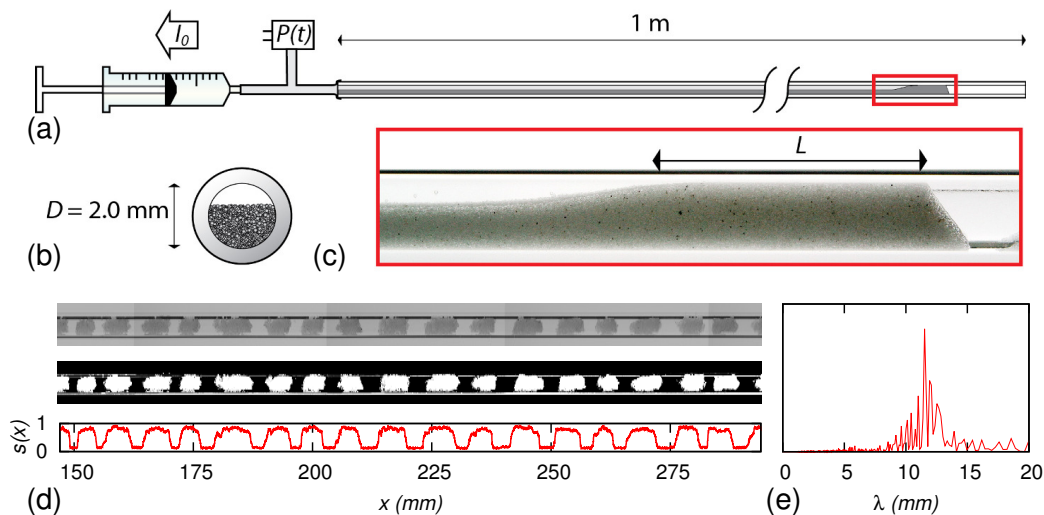
FIG. 1. (a) Schematic of the experimental setup. A syringe pump withdraws water at constant rate I_0 from a horizontal glass tube initially filled with a mixture of water and sedimented grains. Liquid pressure is measured at the tube outlet. (b) Schematic of the tube's intial cross section, and (c) close-up of accumulation front shortly after start of withdrawal. (d) Granular plugs obtained after drainage at low withdrawal rate (top), same picture after thresholding showing granular matter in white (middle), and normalized filling fraction parameter $s(x)$ estimating the density of granular matter from the thresholded picture (bottom). (e) Spatial power spectral density obtained for the signal $s(x)$ as a function of the inverse spatial frequency λ. ($I_0 = 0.1$ mL.min^{-1}, $\varphi \approx 0.5$, $d = [150 - 200]$ μm).

shed by the moving interface, and that the system undergoes a transition from frictional to viscous flow as the flow rate increases.

Figure 1(a) illustrates the experiment: A syringe pump withdraws water at a controlled flow rate I_0 from one end of the horizontal tube, driving invasion of air at atmospheric pressure from the opposite open end. The glass beads form a uniform sedimented layer along the tube with well-defined granular filling fraction $\varphi = \phi_0/\phi_c$, where ϕ_0 is the volume fraction of grains in the grain-water mixture, and ϕ_c corresponds to random close packing in the sedimented layer. φ thus corresponds to the fraction of the tube cross-sectional area taken up by the layer of grains [Fig. 1(b)]. The experiment is imaged against a LED screen, and variations in illumination intensity are corrected by subtracting a reference image. Figure 1(c) shows a close-up of a granular accumulation front, and Fig. 1(d) shows an example of the trail of granular plugs left behind the invading meniscus after the tube is fully drained. Images are thresholded to isolate the granular fraction, and the filling fraction is measured by a normalized variable $s(x,t)$ such that $s = 1$ and 0 for a fully packed and empty tube, respectively, and $s(x, t = 0) = s_0$ corresponds to the initial filling height.

The spatial structure obtained is analyzed with the power spectral density of $s(x)$; see Fig. 1(e). The power spectrum maximum gives a scale $\lambda_0 \simeq 11.5$ mm, and corresponds to the averaged spatial period $\langle L_{plug} + L_{gap} \rangle$ of one plug and one gap. The average plug size measured

after smoothing the function $s(x)$ gives $\langle L_{plug} \rangle \approx 5.9$ mm which is consistent with the maximum $\lambda_0 \approx 2\langle L_{plug} \rangle$ corresponding to an initial filling fraction $\varphi \approx 0.5$.

At a slow withdrawal rate, the viscous pressure drop along the tube is small, such that the pressure imposed by the pump is mainly balanced by the capillary pressure at the gas-liquid-grain interface. As the invading meniscus meets the granular bed, capillary forces act to sweep the grains along, and an accumulation front develops ahead of the interface as seen in Fig. 1(c). Inside the front, stress is transferred through grain-grain contacts, and a portion of the horizontally imposed stress is redirected towards the confining boundaries of the tube. We adopt a Janssen stress distribution model where the redirected stress σ_r is proportional to the applied horizontal stress σ_h, $\sigma_r = K\sigma_h$, where K is the Janssen coefficient [22, 23, 29]. The gas pressure P required to move the accumulation front increases exponentially with the front length L:

$$P \approx \sigma_0(\varphi, \mu, K) \exp(4\mu KL/D), \qquad (1)$$

where μ is the static friction coefficient and the prefactor σ_0 is a function of filling fraction and the frictional properties of the granular material [23, 29, 39].

Figure 2(a) shows close-up images at different stages of formation of a single plug, with Fig. 2(b) representing a spatio-temporal diagram of the filling fraction parameter $s(x,t)$, where time develops from top to bottom. The unperturbed initial sedimented state corresponds to intermediate values of s (gray, upper left). The bright area
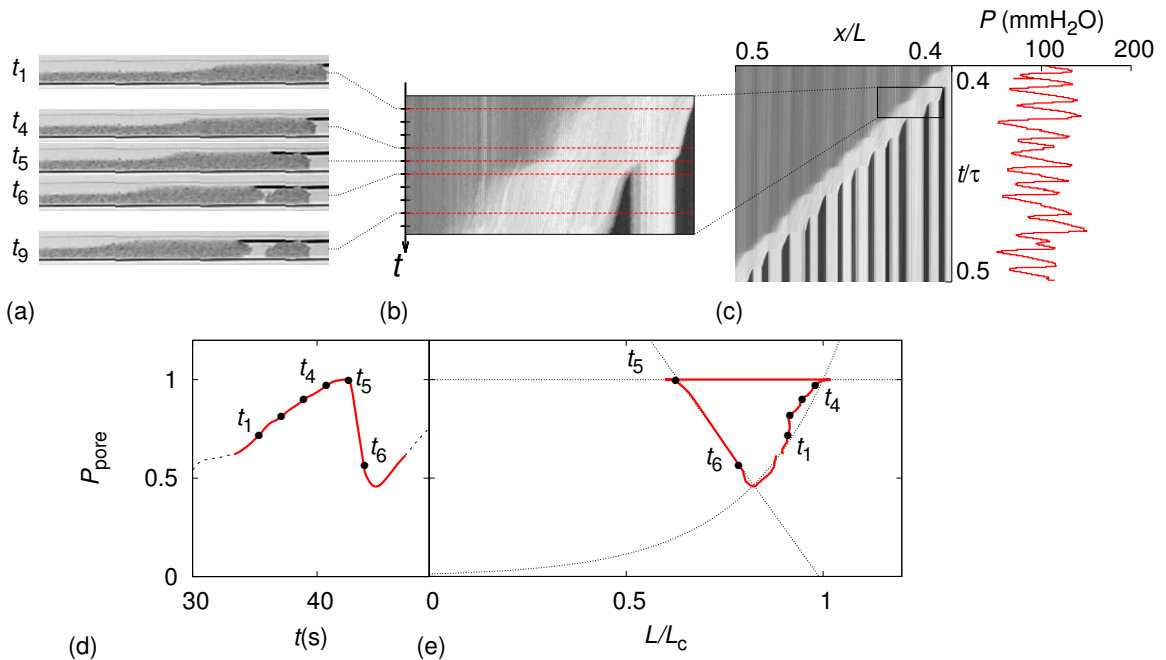
FIG. 2. Plug formation for $I_0 = 0.3$ mL·min^{-1}, $\varphi = 0.5$, and $d = [200 - 300]$ μm. (a) Images and (b) spatiotemporal diagram $s(x,t)$ of the formation of a single plug: slow compaction ($t_1 - t_4$); rapid air percolation with plug splitting ($t_4 - t_5$); viscous slip ($t_5 - t_6$); and the next slow compaction ($t > t_6$). (c) A full $s(x,t)$ diagram over several plug formation cycles with corresponding measured liquid pressure. The pressure increases gradually during the slow compaction phase, then drops rapidly during the slip phase. (d) and (e) Pressure as a function of time and plug length, respectively, for a single plug formation corresponding to (a) and (b). Conceptual trajectory according to Eqs. (1) and (2) (dotted line) plotted together with measured pressure and front length (red line, data markers).

illustrates the motion of the accumulation front, and the plug formation corresponds to the appearance of a vertical, static column flanked by dark zones corresponding to empty tube sections. The system cycles through repeated plug forming events where the moving interface sheds a series of plugs separated by gaps as illustrated in the full spatiotemporal diagram in Fig. 2(c). The interface travels from right to left, and the diagonal outlines the progression of the interface whose speed is given by the slope $\Delta X/\Delta t \propto [4/(\pi D^2)]\Delta V/\Delta t$ determined by the pumping rate $I_0 = \Delta V/\Delta t$, ΔV being the volume withdrawn from the tube during the time interval Δt. The plugs form in an intermittent, stick-slip fashion as evident from the sawtooth pressure curve [Fig. 2(c)], indicating that the dynamics is dominated by frictional interactions.

Figure 2(d) shows the pressure evolution during the formation of the plug depicted in Fig. 2(a), with a corresponding trajectory of pressure versus plug length illustrated in Fig. 2(e). The period t_1 to t_4 corresponds to the slow accumulation or compaction phase where the pressure increases according to Eq. (1). As the accumulation front grows to a critical length L_c, the gas pressure reaches the capillary pore throat pressure, $P_{pore} \propto \gamma/d$, and the meniscus begins to invade the pore space between the grains. γ is the liquid-air interfacial tension, and we assume that typical pore sizes are proportional to average bead diameter d. Air percolates relatively quickly

through the packing (t_4 to t_5), giving rise to a Darcy flow of the displaced water. The flow acts to destabilize the packing, and the plug splits, leaving behind the percolated section as a static plug (t_5).

The meniscus now moves quickly, driven by release of elastic energy stored in the system due to the underpressure in the liquid, and the fluidized granular front grows linearly with decreasing pressure (t_5 to t_6). The decreasing slope $\Delta P/\Delta L$ is given by the system's compressibility, $\beta V_0 = -\Delta V/\Delta P$, where V_0 is the total system volume. Together with the granular material mass balance as sedimented grains accumulate onto the granular front, $\phi_c \Delta L = \phi_0(\Delta L + \Delta X)$, this gives:

$$\frac{\Delta P}{\Delta L} = -\frac{\pi D^2}{4\beta V_0}\frac{\phi_c - \phi_0}{\phi_0}. \tag{2}$$

The motion comes to a halt when the pressure is fully relaxed, and a new cycle of pressure increase and slow accumulation ensues.

Figure 3 illustrates the flow dynamics over 5 orders of magnitude of the withdrawal rate I_0. So far we have considered the slow withdrawal regime where the dynamics is governed by frictional forces ($I_0 \leq 0.1$ mL·min^{-1}). A transitional regime with larger granular fronts and fewer plugs occurs as the withdrawing rate increases ($0.3 \leq I_0 \leq 1$ mL·min^{-1}). The larger pumping rate increases the viscous forces on the granular material. The
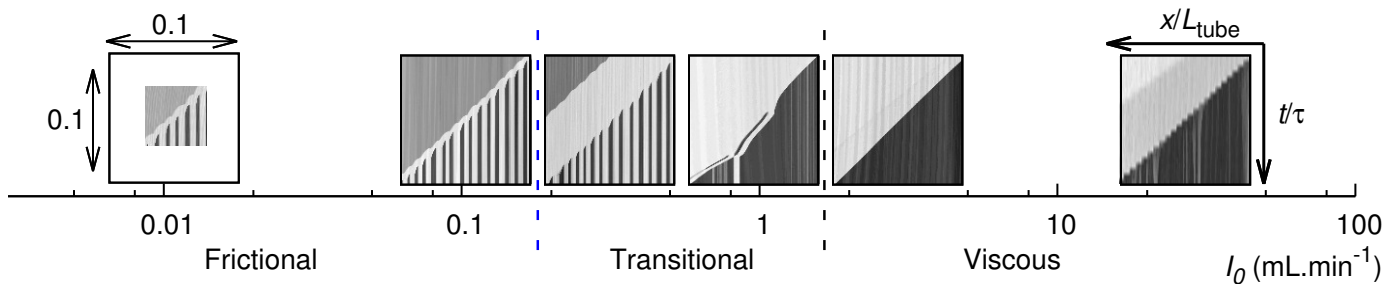
FIG. 3. Spatiotemporal $s(x,t)$ diagrams obtained for different withdrawal rates $I_0 \in [0.01, 30]$ mL·min^{-1}. (Grain size $d = [75, 100]$ μm and $\varphi = 0.50 \pm 0.05$ for all experiments). The diagrams feature reduced units x/L_{tube} and t/τ with $\tau = L_{tube}\pi D^2/(4I_0)$, and display a tenth of the tube's length, $L_{tube}/10$, i.e., a total recording time $\tau/10$, so that enough details are captured. At $I_0 = 0.01$ mL·min^{-1} the recording time was limited to 0.065τ. The dashed lines demarcate the boundaries between frictional, transitional and viscous flow regimes.

granular suspension forms a larger fluidized accumulation front, and the shedding of plugs becomes irregular and infrequent.

Increasing the pumping rate beyond $I_0 \geq 3$ mL·min^{-1} results in a suspended granular phase along the entire length of the tube, and a full evacuation of the granular mixture with no plug formation. The viscous forces dominate the transport regime and no frictional grain-grain contacts have time to form in the fluidized material. Propagating fluctuations of the suspension density explain shades of light levels in the fluidised granular material that can be observed in the $s(x,t)$ diagrams for $I_0 \geq 3$ mL·min^{-1}.

A stability condition for a granular front of plug length L_{plug} can be derived considering a balance between the competing frictional and viscous forces, where the transition from frictional to viscous dynamics upon increased I_0 occurs once the viscous drag exceeds the frictional resistance that must be overcome to move the plug. The fluid pressure due to Darcy flow is

$$\delta P_{visc} = \frac{\eta}{k} \frac{4I_0}{\pi D^2} L_{plug}, \tag{3}$$

where η is the liquid viscosity and the permeability k can be related to average grain size using the Kozeny-Carman equation, $k = (d^2/180)(1-\phi_c)^3/\phi_c^2$.

The gravitationally induced frictional stress associated with an accumulation front of length L_{plug} is given by Eq. (1). The prefactor σ_0 can be expressed as

$$\sigma_0 = D\phi_c\Delta\rho g \left(\left(1 + \cos^2\theta\varphi^2\right) \frac{\mu}{\tan\theta} + \frac{1}{4K} \right), \tag{4}$$

where we have used the expression derived in Ref. [23] adapted for cylindrical confinement [39]. The frictional stress is an increasing function of the filling fraction φ and granular friction μ, θ being the angle of repose, and $\Delta\rho$ the density contrast between grains and liquid.

Plug formation is prevented when fluid forces exceed frictional stress in the plugs. We define a dimensionless number as the ratio between viscous and frictional forces:

$N = \delta P_{visc}/\delta P_{fric}$ such that $N = 1$ marks the transition between plug formation and a fluidized packing. Rearranging Eqs. (1), (3) and (4), we get the following transition flow rate:

$$I_{0,N=1} = \frac{k\pi D^2}{4\eta L_{plug}} \sigma_0 \exp(4\mu K L/D) \tag{5}$$

where the permeability $k \propto d^2$.

The exploration of pumping rates $I_0 \in [0.01 - 30]$ mL·min^{-1} and bead sizes $d \in [50 - 300]$ μm, shows a frictional regime at low pumping rates and large bead sizes, and a viscous regime at large pumping rates and small bead sizes as shown in the phase diagram in Fig. 4. The transition flow rate $I_{0,N=1}$ (5) is plotted together with the experimental results (blue dashed line). The model matches the data well considering the simplistic assumptions. The model assumes maximum friction in jammed plugs which can be considered as an upper limit, and explains the higher transitional flow rates predicted than observed experimentally.

In conclusion, we have demonstrated that three-phase gas-liquid-grain flow in narrow tubes produce complex flow patterns due to the interaction between capillary, frictional and viscous forces. The formation of granular plugs at low flow rate is governed by frictional stress associated with grain-grain and grain-tube contacts. The plug formation cycles through three stages: slow compaction, pore invasion, and viscous slip. Increasing the flow rate results in viscous forces fluidising the packing, and a transition to suspension flow is observed. Reducing the grain size leads to lower permeability and increased fluid pressure on the grains, thus lowering the flow rates required to bring on the transition from frictional to viscous dynamics.

Our results provide new insight into how frictional interactions and competing forces lead to the emergence of complex flow patterning in multiphase flows. The experiment represents a quasi 1D representation of a larger family of flow patterning dynamics occurring in 2D Hele-Shaw flows [26–38], where a similar fluidization
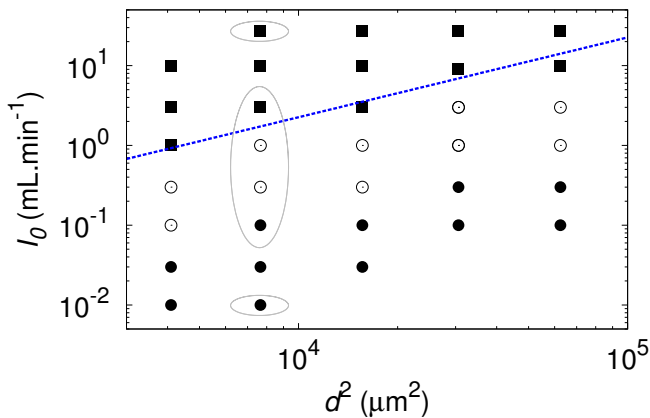
FIG. 4. Phase diagram of I_0 plotted against d^2 featuring the different granular transport regimes observed: Viscous suspension flow (solid squares), frictional plug formation (solid circles), and a transitional regime (open circles). Glass beads were sieved to the following size ranges: $[53 - 75]$, $[75 - 100]$, $[100 - 150]$, $[150 - 200]$, and $[200 - 300]$ μm, with pumping rates ranging from $0.01 - 30$ mL·min^{-1}. Encircled markers correspond to observations in Fig. 3. The blue dashed line represents the theoretical transition flow rate $I_{0,N=1}$ [Eq. 5] where we have used $L_{plug} = 5.9$ mm [Fig. 1 (e)], $\mu = 0.47$ [29], $K = 0.6$ [23], $\theta = 25^o$, $\phi_c = 0.6$, $\Delta\rho = 1.463 \times 10^3$ kg·m^{-3}.

transition is observed [30], and where stick-slip bubbles [30, 31] are analogues to the plug formation observed in the 1D tube system.

———————

* b.sandnes@swansea.ac.uk

[1] D. Gidaspow and J. Huang, Ann. of Biomed. Eng. **37**, 1534 (2009).
[2] J. B. Freund and M. M. Orescanin, J. Fluid Mech. **671**, 466 (2011).
[3] O. Molerus, Powder Technol. **88**, 309 (1996).
[4] F. B. Soeypan, S. Cremaschi, C. Sarica, H. J. Subramani, and G. E. Kouba, AlChE J. **60**, 76 (2014).
[5] J. Tronvoll and E. Fjær, Int. J. Rock Mech. Min. Sci. & Geomech. Abstr. **31**, 393 (1994).
[6] k. A. Triplett, S. M. Ghiaasiaan, S. I. Abdel-Khalik, and D. L. Sadowski, Int. J. Multiphas. Flow **25**, 377 (1999).
[7] M. Suo and P. Griffith, J. Basic Eng **86**, 576 (1964).
[8] L. Cueto-Felgueroso and R. Juanes, Phys. Rev. Lett. **108** 144502 (2012).
[9] M. Houssais, C. P. Ortiz, D. J. Durian, and D.J. Jerol-

mack, Nat. Commun. **6**, 6527 (2015).
[10] M. Strauss, S. McNamara, and H. J. Herrmann, Granul. Matter **9**, 35 (2007).
[11] C.-Y. Wen and H. P. Simons, A.I.Ch.E. Journal **5**, 263 (1959).
[12] J. E. Hilton and P. W. Cleary, Chem. Eng. Sci. **66**, 231 (2011).
[13] O. Durán, B. Andreotti, and P. Claudin Phys. Fluids **24**, 103306 (2012).
[14] A. Fall, F. Bertrand, G. Ovarlez and D. Bonn, Phys. Rev. Lett. **103**, 178301 (2009).
[15] R. Blumenfeld, S. F. Edwards, and M. Schwartz, Eur. Phys. J. E **32**, 333 (2010).
[16] F. Boyer, E. Guazzelli and O. Pouliquen, Phys. Rev. Lett. **107**, 188301 (2011).
[17] R. Seto, R. Mari, J. F. Morris and M. M. Denn, Phys. Rev. Lett. **111**, 218301 (2013).
[18] E. Brown and H. M. Jaeger, Rep. Prog. Phys. **77**, 046602 (2014).
[19] M. Trulsson, B. Andreotti, and P. Claudin, Phys. Rev. Lett. **109**, 118305 (2012).
[20] E. Lerner, G. Düring, and M. Wyart, PNAS **109**, 4798 (2012).
[21] T. S. Majmudar and R. P. Behringer, Nature **435**, 1079 (2005).
[22] H. A. Janssen, Z. Ver. Dtsch. Ing. **39**, 1045 (1895).
[23] B. Marks, B. Sandnes, G. Dumazer, J. A. Eriksen, and K. J. Måløy, Front. Phys. **3**, 41 (2015).
[24] O. Pouliquen and Y. Forterre, Phil. Trans. R. Soc. A **367**, 5091 (2009).
[25] P. G. Rognon, T. Miller, B. Metzger, and I. Einav, J. Fluid Mech. **764**, 171 (2015).
[26] B. Sandnes, H. A. Knudsen, K. J. Måløy, and E. G. Flekkøy, Phys. Rev. Lett. **99**, 038001 (2007).
[27] C. Chevalier, A. Lindner, and E. Clément, Phys. Rev. Lett. **99**, 174501 (2007).
[28] C. Chevalier, A. Lindner, M. Leroux, and E. Clément, J. NonNewton. Fluid **158**, 63 (2009).
[29] H. A. Knudsen, B. Sandnes, E. G. Flekkøy, and K. J. Måløy, Phys. Rev. E, **77**, 021301 (2008).
[30] B. Sandnes, E. G. Flekkøy, H. A. Knudsen, K. J. Måløy, and H. See, Nat. Comm. **2**, 288 (2011).
[31] B. Sandnes, E. G. Flekkøy, and K. J. Måløy, Eur. Phys. J.-Special Topics **204**, 19 (2012).
[32] J. A. Eriksen, B. Marks, B. Sandnes, and R. Toussaint, Phys. Rev. E **91**, 052204 (2015).
[33] R. Holtzman and R. Juanes, Phys. Rev. E **82**, 046305 (2010).
[34] F. Stauffer, X.-Z. Kong, and W. Kinzelbach, Adv. in Water Res. **32**, 1180 (2009).
[35] G. Varas, V. Vidal, and J.-C. Geminard, Phys. Rev. E **83**, 011302 (2011).
[36] R. Holtzman, M. L. Szulczewski, and R. Juanes, Phys. Rev. Lett. **108**, 264504 (2012).
[37] A. Islam, S. Chevalier, I. B. Salem, Y. Bernabe, R. Juanes, and M. Sassi, Int. J. Multiphase Flow **58**, 279 (2014).
[38] J. Oppenheimer, A. C. Rust, K. V. Cashman, and B. Sandnes, Front. Phys. **3**, 60 (2015).
[39] See Supplemental Material at [URL will be inserted by publisher] for detailed derivation of the frictional stress.